Uniting superior mechanical properties with oxidation resistance in a refractory high-entropy alloy via Cr and Al alloying

Dingcong Cui [a], Xin Liu [a], Zhongsheng Yang [a], Bojing Guo [a], Zhijun Wang [a], Junjie Li [a], Jincheng Wang [a,*], Feng He [a,b,c,*]

[a] *State Key Laboratory of Solidification Processing, Northwestern Polytechnical University, Xi'an 710072, China*
[b] *Research & Development Institute of Northwestern Polytechnical University in Shenzhen, Shenzhen 518063, China*
[c] *Collaborative Innovation Center of Northwestern Polytechnical University, Shanghai 201100, China*

ABSTRACT

Refractory high-entropy alloys (RHEAs) have attracted considerable interest due to their elevated melting points and remarkable softening resistance. Nevertheless, the ambient-temperature brittleness and inadequate high-temperature oxidation resistance commonly limit the application of the body-centered-cubic (BCC) RHEAs. In this study, we achieved a $Ti_{41}V_{27}Hf_{11.5}Nb_{11.5}Cr_3Al_6$ RHEA with a desirable yield strength of ~1178 MPa and tensile ductility of ~19.5 %. Exploring the underlying mechanisms, we demonstrated that Cr and Al alloying induced a nanoscale spinodal structure and generated a significant lattice misfit, resulting in a notable strengthening effect and pinning behavior. Meanwhile, dislocation configurations involving loops and cross slips were stimulated by pinning, serving a reliable strain-hardening capability to large strains. Significantly, Cr and Al alloying improved oxidation resistance and prevented severe spallation at high temperatures by forming protective oxide layers. These results provide opportunities to design novel RHEAs.

Refractory high-entropy alloys (RHEAs), a subgroup of extensively alloyed systems, have garnered increasing attention due to their capacity to retain significant yield strength under extremely elevated temperatures [1–3]. Yet several serious obstacles exist in the RHEAs with body-centered-cubic (BCC) structures [4,5]. First, the Achilles' heel of most BCC RHEAs is their negligible tensile ductility at ambient temperature. For instance, NbMoTaW and VNbMoTaW only exhibit fracture strain of about 2 % under ambient compression tests [6]. Second, many discovered that RHEAs suffer from poor oxidation resistance, like pure refractory metals, owing to substantial scale spallation or even complete oxidation at elevated temperatures [7,8]. Adding oxidation-resistant elements (e.g., aluminum (Al), chromium (Cr), and silicon (Si)) to RHEAs is a promising path to achieve high-temperature oxidation resistance [9,10]. However, Al, Cr, and Si elements exhibit chemical activity with refractory metallic elements and commonly promote the formation of brittle phase, degrading the room temperature ductility [11,12]. Consequently, the RHEA rush has led to a few alloys exhibiting application-worthy mechanical performances.

Recently, Wei et al. [13] designed $Ti_{38}V_{15}Nb_{23}Hf_{24}$ RHEAs with as-cast tensile ductility exceeding 20 % and yield strength reaching 800 MPa. However, the catch is that this system's yield strength and oxidation resistance are insufficient. In the case of the former, the spinodal structure induced by a high absolute value of mixing enthalpy (ΔH_m) can greatly increase the strength of RHEAs [14,15]. This enhancement can be achieved by alloying with certain metallic elements like Al [16]. Regarding the latter case, Ouyang et al. [17] reported that $Ti_{38}V_{15}Nb_{23}Hf_{24}$ RHEA cannot form a dense passivation oxide layer to prevent the rapid diffusion of oxygen. The protective oxide layers, such as Cr_2O_3 and Al_2O_3, are the prerequisite to achieving an outstanding oxygen-shielded capability [18].

In this study, we took advantage of the intrinsic characteristics of Cr and Al elements to develop a novel RHEA with superior mechanical properties and improve its oxidation resistance. Initially, we adopted an updated $Ti_{41}V_{27}Hf_{16}Nb_{16}$ RHEA as the ductile base alloy. This choice mitigates the likelihood of brittle phase formation by decreasing the Hf content [19]. Supplementary Table. S1 illustrates the ΔH_m between the atom pairs. The values of ΔH_m are pretty large for the atom pairs involving the refractory element (Ti, V, Hf, or Nb) and Cr/Al element [20]. Hence, alloying with appropriate Cr and Al in this alloy can probably introduce spinodal structure and improve oxidation resistance.

---

* Corresponding authors.
E-mail addresses: jchwang@nwpu.edu.cn (J. Wang), fenghe1991@nwpu.edu.cn (F. He).

Supplementary Table. S2–3 provides empirical phase prediction parameters for HEAs. The brittle behavior tends to happen when Cr content is over 6 at.% owing to a large valence electron concentration (VEC > 4.5) [21]. According to the previous research, the ductility would be reduced in the AlHfNbTiZr RHEA when the Al content surpasses 7 at.% [22]. Overall, our investigation focused on the mechanical properties and oxidation resistance of the $Ti_{41}V_{27}Hf_{16}Nb_{16}$ RHEA, with the addition of Cr and Al ($\leq$6 at.%).

$Ti_{41}V_{27}Hf_{16}Nb_{16}$ (at.%, denoted as base RHEA) and $Ti_{41}V_{27}Hf_{16-(x+y)/2}Nb_{16-(x+y)/2}Cr_xAl_y$ (where $x = 3, 6; y = 6$) were prepared in a water-cooled copper crucible by vacuum arc melting, and their ingots were remelted five times to ensure chemical homogeneity. The purity of every alloying element exceeded 99.9 wt.%. Crystalline structures were identified using X-ray diffractometry (XRD) (X'Pert PRO) with Cu-Kα radiation at a scanning rate of 2°/min. The samples intended for scanning electron microscopy (SEM), energy dispersive spectrometer (EDS), and electron backscattered diffraction (EBSD) characterization were ground to 4000-grit SiC paper and polished with SiO_2 suspension, then characterized by TESCAN MIRA-III equipped with EBSD/EDS detector. Aztec-HKL software was employed for grain size analysis. The samples for transmission electron microscope (TEM) observation were mechanically ground to ~40 μm thickness, followed by ion milled, and finally identified by a double Cs corrector TEM (Themis Z).

Ambient-temperature uniaxial tensile testing was conducted on a TSMT mechanical testing platform at a strain rate of 1×10^{-3} s^{-1}. The tensile specimens with a gauge geometry of 12.5 mm × 3.0 mm × 2.0 mm were sectioned using electrical discharging. At least three specimens were tested for each composition to confirm the reproducibility. Before being tested for digital image correlation (DIC) analyses, the speckle patterns were coated on the surface of the tensile sample, and the resulting deformed characteristics were captured by a high-speed camera (frame rate, 1 Hz). Zeiss Inspect Correlate software was used to calculate the local strain profiles during the DIC experiment. The oxidation resistance of the alloys was assessed at 800 and 1000 °C, with exposure times of 2, 4, 6, and 10 h in an ambient air environment.

We first examined the ambient-temperature tensile properties of these RHEAs. As presented in Fig. 1, the base RHEA possesses a yield strength (σ_y) of 953 ± 23 MPa with a fracture elongation (ε_f) of 25.2 ± 0.2 %. Alloying with 3 at.% Cr enhances the tensile properties of the base RHEA, while 6 at.% Cr embrittles the alloy (see the engineering stress-strain curves of RHEAs alloying with Cr in Supplementary Fig. S1). We proceeded to alloy with 6 at.% Al in the $Ti_{41}V_{27}Hf_{14.5}Nb_{14.5}Cr_3$ RHEA. The σ_y of the obtained $Ti_{41}V_{27}Hf_{11.5}Nb_{11.5}Cr_3Al_6$ RHEA (denoted as CrAl) exhibited a significant increase of almost 24 %, reaching a value of 1178 ± 11 MPa. Notably, this increase in σ_y was achieved without

compromising its tensile ductility ($\varepsilon_f = 19.5 \pm 1.4$ %). SEM images of the fractured surface show dimples (see inset in Fig. 1(a)), indicating a ductile manner. After conducting a comparative analysis of the present RHEAs with other RHEAs [5,15,23-29], it becomes apparent that CrAl demonstrates an unprecedented combination of yield strength and tensile ductility in the as-cast state (refer to Fig. 1(b)).

The insight into the relationships between microstructure and mechanical response will provide a fundamental basis for the performances. The EBSD-IPF maps and XRD curves (Supplementary Fig. S2) indicate that the base and CrAl RHEAs display a fully equiaxed grain morphology with BCC-phase constitution. Fig. 2(a-c) illustrates the high-angle annular dark field-scanning transmission electron microscope (HAADF-STEM) micrographs of CrAl under the [111] zone axis. The plate-like nanoscale phases (β^*) with dimensions of 20~300 nm in length come into being, exhibiting varying contrast and featuring a diffusional transition zone instead of a clearly defined interface. The variation in image contrast can be attributed to the Z-contrast of the regions rich in light or heavy atoms (Fig. 2(d-f)) [30]. Therefore, the brighter contrast of β^* is due to the concentration of the Hf element, which has a more significant atomic number than the others. Laube et al. [31] found a sharp interface between the decomposed phases in another Al-containing RHEA, indicating a phase nucleation and growth mechanism. The blurred boundary dominated by 'uphill' diffusion in CrAl should be a case of spinodal decomposition.

The associated fast Fourier transform (FFT) patterns in Fig. 2(c) confirm that both indicated regions correspond to BCC phases, revealing the characteristic of spinodal decomposition in CrAl, a phenomenon not seen in the base RHEA (Supplementary Fig. S3). Fig. S3 shows no evident chemical heterogeneity or second phase in the base RHEA. Hence, introducing Cr and Al atoms facilitates the development of spinodal structure. Additionally, FFT patterns have not yet exhibited extra discs, indicating the lack or insignificance of long-range/short-range ordering (L/SRO). According to XRD results in Supplementary Fig. S2(c-d), the (200) diffraction peak of CrAl shows a sideband due to the decomposed phases and the periodic difference of their lattice parameters. The lattice parameters of the matrix phase (β) and β^* can be calculated to be 3.273 Å and 3.258 Å, respectively, exhibiting a misfit of 0.44 %.

As depicted in Fig. 3(a-b), the shear strain (e_{xx}) of the spinodal structure was mapped using the geometric phase analysis (GPA) method [32]. The definition of the strain is with respect to the undistorted lattice [33]. The β^* phase resulted in an inhomogeneous strain distribution, with the highest strain at the coherent interface with the β phase. On the one hand, spinodal structure enhanced the chemical heterogeneity, thus increasing the lattice distortion (from XRD analysis and GPA mapping) and influencing the strengthening mechanisms. On the other hand, the spinodal structure created a high density of diffusive boundaries, which
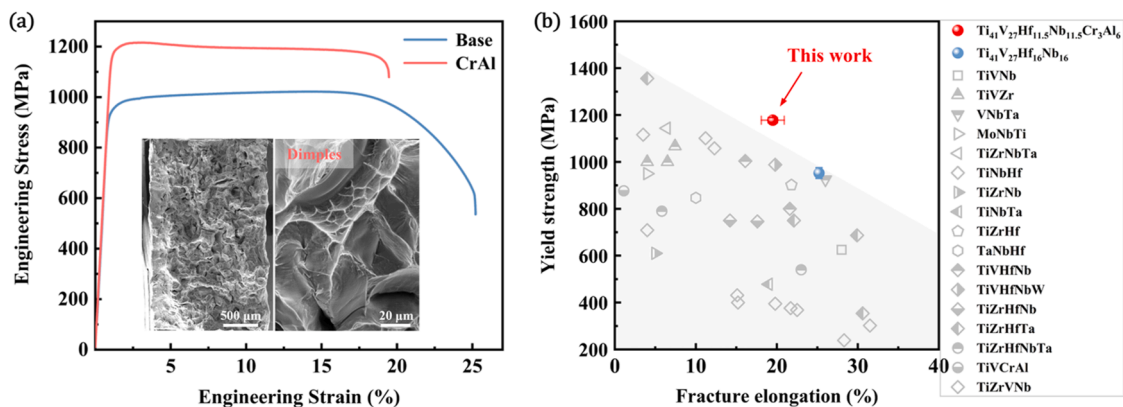

Fig. 1. The tensile strength-ductility combination achieved in the $Ti_{41}V_{27}Hf_{16}Nb_{16}$ and $Ti_{41}V_{27}Hf_{11.5}Nb_{11.5}Cr_3Al_6$ RHEAs at room temperature. (a) Engineering stress-strain curves with SEM images of the fracture surface of CrAl in the inset. (b) Tensile yield strength versus fracture elongation, compared with the previously reported BCC RHEAs [5,15,23–29].
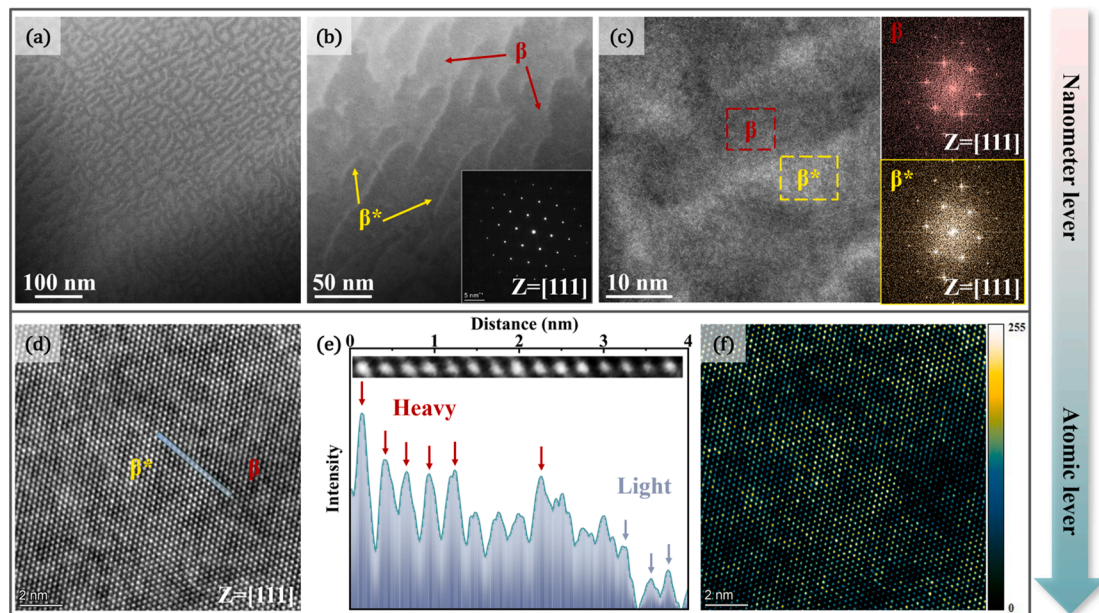
Fig. 2. Microstructure of the CrAl RHEA. (a) HAADF-STEM image showing nanoscale spinodal structure. (b) Spinodal phases (β^*) distribute in the matrix (β). (c) β^* and β phases show the same BCC crystal structures (see the selected area electron diffraction patterns). (d) Atomic-resolution HAADF-STEM image showing coherency at the β and β^* interface. (e) Zoom-in image of the blue square region in (d), showing varying intensity from atomic column to column. (f) Intensity color map for the atomic columns corresponding to (d).
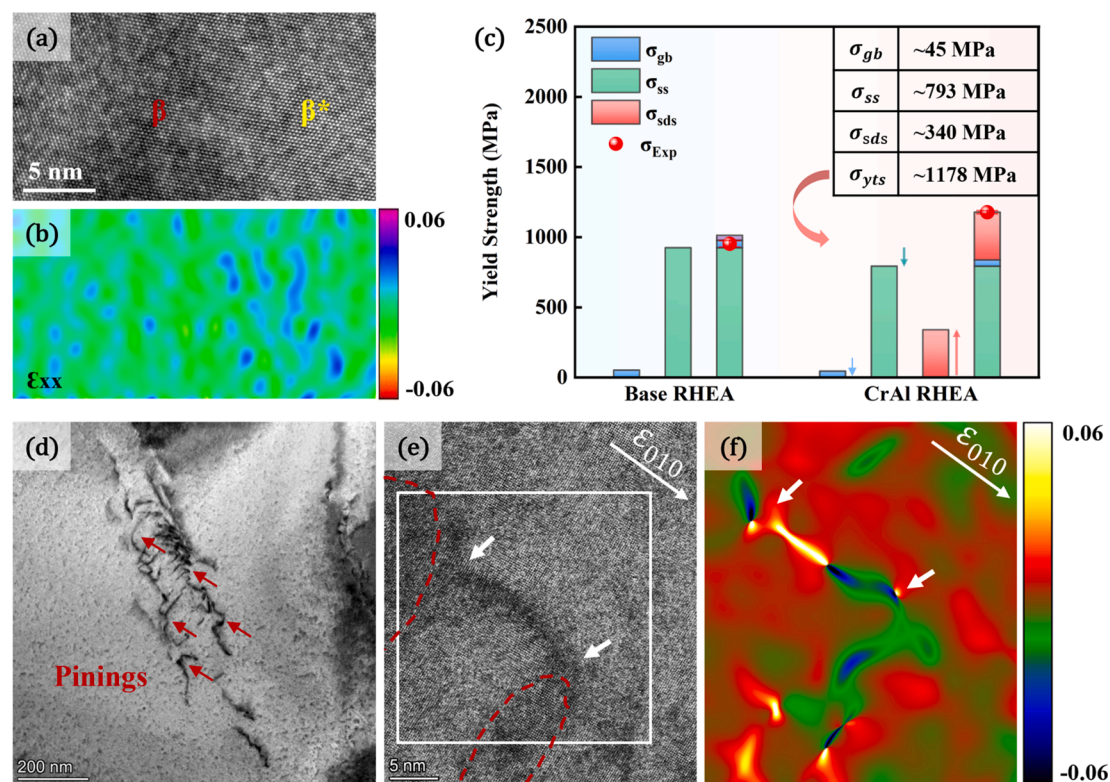

Fig. 3. Lattice strain mapping and impact mechanisms of spinodal structure in the CrAl RHEA. (a) Magnified HAADF-STEM image of the spinodal structure. (b) The corresponding strain distribution before tensile deformation calculated by geometric phase analysis (GPA). (c) Estimated yield strength of the base and CrAl RHEAs caused by the solid solution strengthening (σ_{ss}), grain boundary strengthening (σ_{gb}), and spinodal-decomposition strengthening (σ_{sds}). The corresponding experimental yield tensile strengths (σ_{yts}) are marked by red dots. The inset indicates that σ_{sds} provides the enhanced yield tensile of CrAl. (d) Dislocation pinning in the 2 % deformed CrAl RHEA. (e) Pining points (marked as the white arrows) at the interface between β and β^* phases (marked as the red dotted lines). (f) Lattice strain distribution around the pinning points in (e). (For interpretation of the references to color in this figure legend, the reader is referred to the web version of this article.).

acted as effective barriers to dislocation motion [34].

Based on the acknowledged solid-solution strengthening models proposed by Maresca's model [35] and Kato's model [36] for spinodal-modulated BCC alloys, we calculated the theoretical σ_y of both RHEAs considering solid solution strengthening (σ_{ss}) contributed by the alloying elements, Hall-Petch strengthening (σ_{gb}) resulting from the grain refinement, and spinodal-decomposition strengthening (σ_{sds}). Fig. 3(c) illustrates the enhancement from these mechanisms (detailed in Notes. 1). Alloying with Cr and Al decreases σ_{ss} by ~132 MPa and σ_{gb} by ~7 MPa. The increased σ_{yts} in CrAl is attributed to the effective σ_{sds} (~340 MPa). Due to the existence of micro-segregations (**Fig. S2**), we should note potential discrepancies in σ_{sds}. According to research on spinodal-modulated $Ti_{41}V_{27}Hf_{15}Nb_{15}O_2$ RHEA, it has been reported that the large lattice misfit of 0.59 % generated by β and β* phases can provide lattice misfit strengthening (~293 MPa) for σ_{sds} [15]. CrAl achieves a comparable lattice misfit of 0.44 %, the dominating factor for enhancing yield strength.

The spinodal strengthening fundamentally linked to the β/β* interface. TEM observations of deformed CrAl at 2 % strain (Fig. 3(d-e)) revealed the interaction between dislocations and spinodal structure. The dispersed high-strain regions in Fig. 3(f) correspond to the spinodal interfaces, showing large elastic strains due to the atomic mismatch. As such, an unusually rugged landscape is introduced, enhancing the resistance to dislocation motion [37]. The conventional wisdom holds that the energy would be relaxed through crack propagation if the dislocation activity remains inactive [38,39]. As a result, pinning typically increases the strength by promoting dislocation multiplication at the expense of ductility [40]. The promising ductility of CrAl calls for a deeper assessment of the underlying deformation mechanisms.

Fig. 4(a) plots the normalized strain-hardening rate (SHR) versus the true strain curves of CrAl. After experiencing a decline in stage I (0–5%), the SHR continuously increases throughout stage II (approximately 5–10 %), temporarily stabilizing in stage III and exhibiting a reduction until the fracture occurs. As shown in Fig. S4, this well-developed SHR is responsible for high tensile ductility, which is rarely observed in other RHEAs [25,26,41]. TEM investigations were performed to understand the origin of SHR from a plastic-flow perspective. The macro digital image correlation (DIC) analyses prove that deformed CrAl exhibits a non-uniform strain distribution during tension (Fig. 4(b)). To guarantee precision, TEM samples were prepared by subjecting them to incremental tensile strains in accordance with the strain profile.

Now, let us return to the deformation mechanisms of CrAl. In stage I, planar slips prevail, accompanied by abundant wavy dislocations (Fig. 4(c)). There are two conceivable reasons for the coexistence of planar and wavy dislocations. First, the spinodal interfaces act as obstructive agents and cause dislocation pinning. The heavily curved dislocations may represent the local bow-out at discrete pinning points [42]. Second, when dislocations with screw type in the planar slips reach high-stress levels, cross slips are facilitated owing to the strain effect [43]. The cross-slip easily produced a wavy dislocation morphology [44]. In stage II (Fig. 4(d)), cross-slip can contribute to obstacle bypass, enabling more efficient utilization of undeformed regions and promoting deformation delocalization [45]. Meanwhile, a significant quantity of dislocation loops were present at 7 % strain, as evidence of dislocation multiplication from pinning [14]. The pinning and de-pinning process of dislocation reportedly produced loops and glissile dislocations [46]. Cross-slip and pinning alone were insufficient for dislocation multiplication. The formed dislocation junctions acted as new sources for generating mobile dislocations, effectively giving rise to a rising SHR. Similar dislocation configurations that can increase the dislocation density were also found
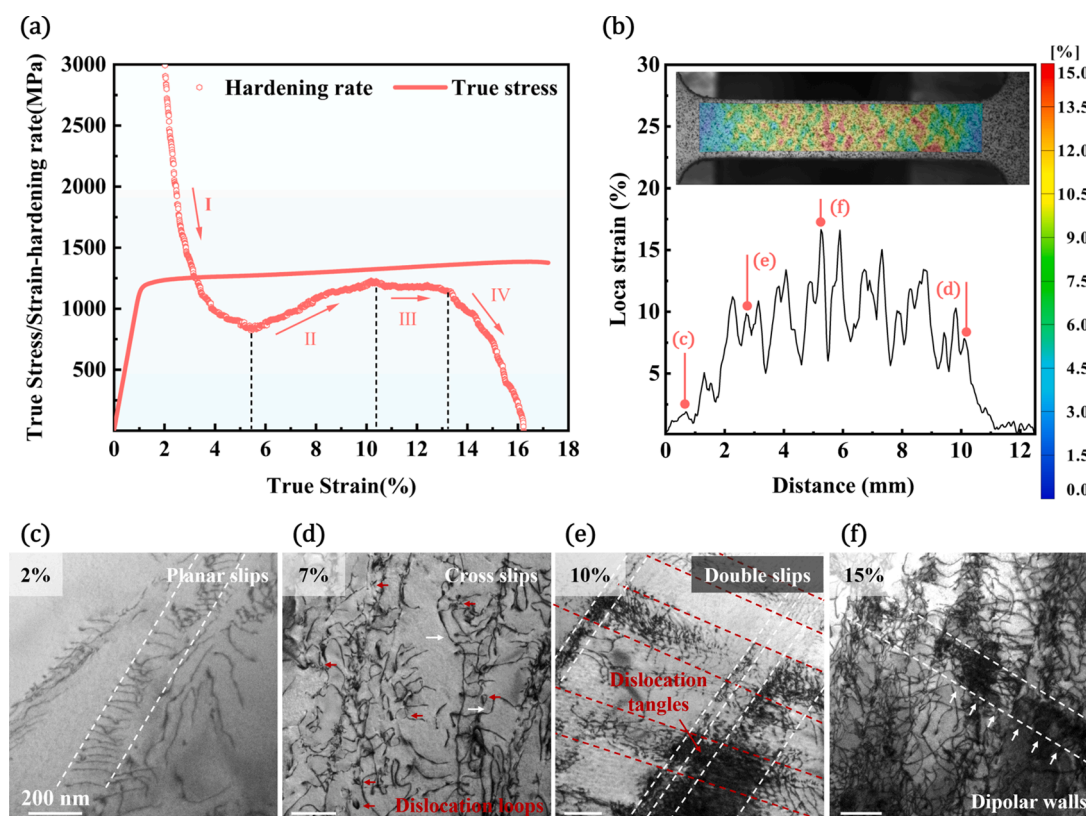

Fig. 4. Mechanical behavior and dislocation evolution of the CrAl RHEA during plastic deformation. (a) True stress-strain curve and plot of strain-hardening rate for the CrAl RHEA. (b) The local strain distribution for a typical tensile sample. The samples at different strains for TEM characterization are extracted from the corresponding positions (marked as red lines). (c-f). Evolution of dislocation patterns. (c) Planar slips at 2 % strain. (d) Cross slips (marked as white arrows) and dislocation loops (marked as red arrows) at 7 % strain. (e) Double slips and formed dislocation tangles (marked as a red arrow) at 10 % strain. (f) Dipolar walls are full of dislocation tangles at 15 % strain. (For interpretation of the references to color in this figure legend, the reader is referred to the web version of this article.).

in the TiZrHfNb RHEAs [38]. Fig. 4(e) highlights the proliferation of second-generation slip bands. Double slips provide opportunities for dislocation intersection and sow dislocation tangles, thereby compensating for the reduction in SHR caused by cross-slips (stage III) [47]. In stage IV, the dislocation pattern behaves like dipolar walls full of dislocation tangles (Fig. 4(f)) [48]. As such, the combined effects of dislocation multiplication, delocalization, and patterning jointly lead to the favorable SHR and ductility. Moreover, we note that alloying with trace interstitial elements (oxygen or nitrogen) can deliver a spinodal-decomposition strengthening, like in $(TiZrNbTa)_{99.1}N_{0.9}$ [49] and $(TiVHfNb)_{98}O_2$ [15], while leading to significant deterioration of the ductility. These results revealed that the advantages of Cr and Al alloying are reflected in maintaining ductility even beyond gigapascal stresses.

The investigation includes an assessment of the oxidation resistance of the RHEAs (exposed to air at 800 and 1000 °C). The mass change curves in Fig. 5(a) indicate that CrAl exhibits consistently lower mass

gain than base RHEA as the exposure temperature and time increase. Correspondingly, the samples exposed at 1000 °C demonstrated that CrAl could maintain structural integrity for up to 6 h. Conversely, the base alloy experienced severe spallation under identical conditions (Fig. 5(b)). RHEA oxide layers at 1000 °C-2 h were selected and investigated. As depicted in Fig. 5(c), XRD patterns demonstrate the presence of mixed oxides consisting of TiO_2, Nb_2O_5, HfO_2, and $TiNb_2O_7$ in the base alloy. In contrast, there exist extensive diffraction peaks of Cr_2O_3 and Al_2O_3 in CrAl. As a result, the thickness of the oxidation layer is much thinner for CrAl (~383 μm) compared with the base alloy (~800 μm), as shown in Fig. 5(d-e). Refractory elements tend to generate porous or volatile oxide scales, making oxygen diffuse into the alloy [18]. As such, Ti, V, Hf, Nb, and O are evenly distributed within the oxide scales of both alloys. Cr_2O_3 and Al_2O_3 scales can enable the inhibition of oxygen dissolution and metallic ion external diffusion [8]. That is, the formed Cr_2O_3 and Al_2O_3 retard the rapid growth of the outer scale and postpone spallation in CrAl.
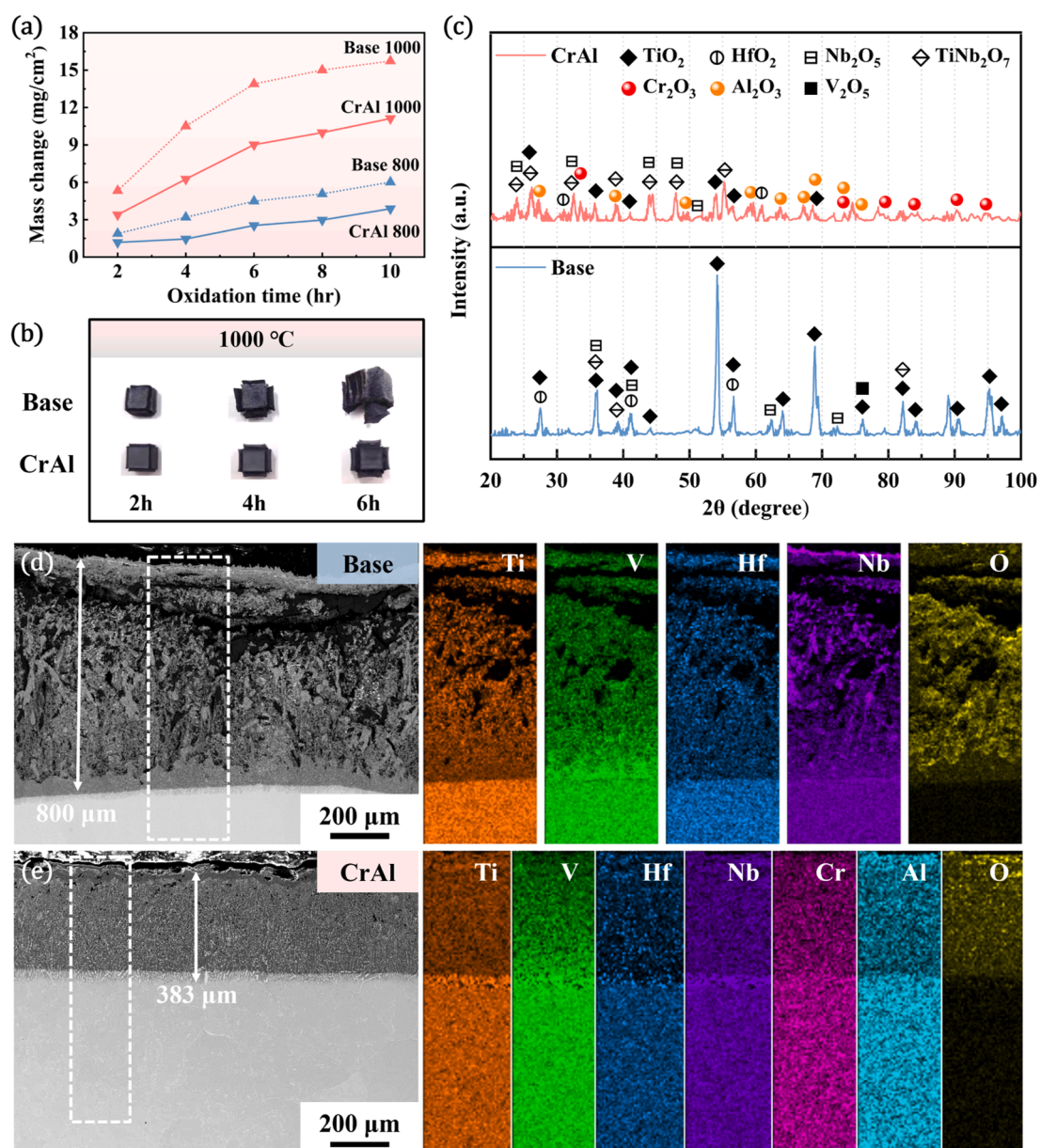

Fig. 5. Oxidation resistance of the base and CrAl RHEAs. (a) The mass gain versus exposure time at different temperatures (800 °C and 1000 °C). (b) The morphologies of two RHEAs after 2 h, 4 h, and 6 h exposure at 1000 °C. (c) XRD patterns of the RHEAs after 1000 °C-2 h oxidation. The cross-sectioned microstructures of 1000 °C-2 h oxidized (d) base and (e) CrAl RHEAs. The element maps were measured by EDS.

RHEAs containing Hf element frequently show suboptimal resistance to oxidation. Sheikh et al. [7] reported Ti$_{1.5}$ZrTa$_{0.5}$Hf$_{0.5}$Nb$_{0.5}$ suffers pesting failure within the temperature range of 600–1000 °C, where the bulk alloy disintegrates into powders. In contrast, catastrophic oxidation has not been seen in CrAl. However, the mass gain gradually increases with time (Fig. 5(b)). The formed oxide scales in CrAl cannot completely prevent the diffusion of oxygen and will continuously grow into the matrix until the alloy is fully oxidized. Oxygen-shielded ability is the necessity for further improving this alloy system's oxidation resistance.

In summary, we investigated how mechanical properties and oxidation resistance can be successfully improved for a class of RHEAs. Via composition modulation, we put alloying with appropriate Cr and Al to generate a nanoscale spinodal structure and enhance yield strength to 1178 MPa. Meanwhile, dislocation configurations were induced by the pinning impact of the spinodal structure. Dislocation intersection and delocalization guaranteed an excellent working hardening ability and thus obtained the elongation of ~19.5 %. The improved oxidation resistance of CrAl RHEA at 1000 °C can be attributed to the formation of protective Cr$_2$O$_3$ and Al$_2$O$_3$ layers, which mitigated severe spallation. These findings accelerate the development of spinodal-modulated RHEAs and provide a new candidate for structural RHEAs.

Declaration of competing interest

The authors declare that they have no known competing financial interests or personal relationships that could have appeared to influence the work reported in this paper.

Acknowledgement

Supplementary materials

Supplementary material associated with this article can be found, in the online version, at doi:10.1016/j.scriptamat.2024.116031.

References

[1] O.N. Senkov, J.M. Scott, S.V. Senkova, F. Meisenkothen, D.B. Miracle, C.F. Woodward, Microstructure and elevated temperature properties of a refractory TaNbHfZrTi alloy, J. Mater. Sci. 47 (9) (2012) 4062–4074.

[2] C. Lee, G. Kim, Y. Chou, B.L. Musico, M.C. Gao, K. An, G. Song, Y.C. Chou, V. Keppens, W. Chen, P.K. Liaw, Temperature dependence of elastic and plastic deformation behavior of a refractory high-entropy alloy, Sci. Adv. 6 (37) (2020) 12.

[3] R. Feng, B.J. Feng, M.C. Gao, C. Zhang, J.C. Neuefeind, J.D. Poplawsky, Y. Ren, K. An, M. Widom, P.K. Liaw, Superior high-temperature strength in a supersaturated refractory high-entropy alloy, Adv. Mater. 33 (48) (2021) 9.

[4] L. Wang, J. Ding, S. Chen, K. Jin, Q. Zhang, J. Cui, B. Wang, B. Chen, T. Li, Y. Ren, S. Zheng, K. Ming, W. Lu, J. Hou, G. Sha, J. Liang, L. Wang, Y. Xue, E. Ma, Tailoring planar slip to achieve pure metal-like ductility in body-centred-cubic multi-principal element alloys, Nat. Mater. 22 (2023) 950–957.

[5] Z. Wang, S. Chen, S. Yang, Q. Luo, Y. Jin, W. Xie, L. Zhang, Q. Li, Light-weight refractory high-entropy alloys: a comprehensive review, J. Mater. Sci. Technol. 151 (2023) 41–65.

[6] O.N. Senkov, G.B. Wilks, J.M. Scott, D.B. Miracle, Mechanical properties of Nb25Mo25Ta25W25 and V20Nb20Mo20Ta20W20 refractory high entropy alloys, Intermetallics 19 (5) (2011) 698–706.

[7] S. Sheikh, M.K. Bijaksana, A. Motallebzadeh, S. Shafeie, A. Lozinko, L. Gan, T.K. Tsao, U. Klement, D. Canadinc, H. Murakami, S. Guo, Accelerated oxidation in ductile refractory high-entropy alloys, Intermetallics 97 (2018) 58–66.

[8] F. Müller, B. Gorr, H.-J. Christ, J. Müller, B. Butz, H. Chen, A. Kauffmann, M. Heilmaier, On the oxidation mechanism of refractory high entropy alloys, Corrosion Sci. 159 (2019) 108161.

[9] X. Pei, Y. Du, H. Wang, T. Li, M. Hu, H. Wang, W. Liu, Effects of Al/Si on the oxidation behavior of a TiZrV0.5Nb0.5 refractory high entropy alloy at 1000 °C, Corrosion Sci. 224 (2023) 111527.

[10] Z. Zhou, X. Peng, W. Lü, S. Yang, H. Li, H. Guo, J. Wang, Ultra-high temperature oxidation resistant refractory high entropy alloys fabricated by laser melting deposition: Al concentration regulation and oxidation mechanism, Corrosion Sci. 221 (2023) 111537.

[11] Z.Q. Xu, Z.L. Ma, Y. Tan, X.W. Cheng, Designing TiVNbTaSi refractory high-entropy alloys with ambient tensile ductility, Scr. Mater. 206 (2022) 6.

[12] X. Huang, J. Miao, A.A. Luo, Order-disorder transition and its mechanical effects in lightweight AlCrTiV high entropy alloys, Scr. Mater. 210 (2022) 114462.

[13] S.L. Wei, S.J. Kim, J.Y. Kang, Y. Zhang, Y.J. Zhang, T. Furuhara, E.S. Park, C.C. Tasan, Natural-mixing guided design of refractory high-entropy alloys with as-cast tensile ductility, Nat. Mater. 19 (11) (2020) 1175–1181.

[14] Y. Chen, Y. Fang, R. Wang, Y. Tang, S. Bai, Q. Yu, Achieving high strength and ductility in high-entropy alloys via spinodal decomposition-induced compositional heterogeneity, J. Mater. Sci. Technol. 141 (2023) 149–154.

[15] D. Cui, Y. Zhang, L. Liu, Y. Li, L. Wang, Z. Wang, J. Li, J. Wang, F. He, Oxygen-assisted spinodal structure achieves 1.5GPa yield strength in a ductile refractory high-entropy alloy, J. Mater. Sci. Technol. 157 (2023) 11–20.

[16] S. Zeng, Y. Zhou, H. Li, H. Zhang, H. Zhang, Z. Zhu, Microstructure and mechanical properties of lightweight Ti3Zr1.5NbVAlx (x = 0, 0.25, 0.5 and 0.75) refractory complex concentrated alloys, J. Mater. Sci. Technol. 130 (2022) 64–74.

[17] D. Ouyang, Z.-J. Chen, H.-B. Yu, K.C. Chan, L. Liu, Oxidation behavior of the Ti38V15Nb23Hf24 refractory high-entropy alloy at elevated temperatures, Corrosion Sci. 198 (2022) 110153.

[18] B. Gorr, S. Schellert, F. Muller, H.J. Christ, A. Kauffmann, M. Heilmaier, Current status of research on the oxidation behavior of refractory high entropy alloys, Adv. Eng. Mater. 23 (5) (2021) 14.

[19] S. Sheikh, S. Shafeie, Q. Hu, J. Ahlström, C. Persson, J. Veselý, J. Zýka, U. Klement, S. Guo, Alloy design for intrinsically ductile refractory high-entropy alloys, J. Appl. Phys. 120 (16) (2016) 164902.

[20] A. Takeuchi, A. Inoue, Classification of bulk metallic glasses by atomic size difference, heat of mixing and period of constituent elements and its application to characterization of the main alloying element, Mater. Trans. 46 (12) (2005) 2817–2829.

[21] J.W. Yeh, Alloy design strategies and future trends in high-entropy alloys, Jom 65 (12) (2013) 1759–1771.

[22] Y.D. Wu, J.J. Si, D.Y. Lin, T. Wang, W.Y. Wang, Y.D. Wang, Z.K. Liu, X.D. Hui, Phase stability and mechanical properties of AlHfNbTiZr high-entropy alloys, Mater. Sci. Eng. A. 724 (2018) 249–259.

[23] S. Zhang, X. Ding, X. Gao, R. Chen, W. Cao, Y. Su, J. Guo, Dual enhancement in strength and ductility of Ti-V-Zr medium entropy alloy by fracture mode transformation via a heterogeneous structure, Int. J. Plast. 160 (2023) 103505.

[24] W. Huang, J. Hou, X. Wang, J. Qiao, Y. Wu, Excellent room-temperature tensile ductility in as-cast Ti37V15Nb22Hf23W3 refractory high entropy alloys, Intermetallics 151 (2022) 107735.

[25] D. Cui, Z. Yang, B. Guo, L. Liu, Z. Wang, J. Li, J. Wang, F. He, Microstructures and mechanical properties of a precipitation hardened refractory multi-principal element alloy, Intermetallics 151 (2022) 107727.

[26] Z.H. Han, L.K. Meng, J. Yang, G. Liu, J.G. Yang, R. Wei, G.J. Zhang, Novel BCC VNbTa refractory multi-element alloys with superior tensile properties, Mater. Sci. Eng. A. 825 (2021) 4.

[27] O.N. Senkov, D.B. Miracle, S.I. Rao, Correlations to improve room temperature ductility of refractory complex concentrated alloys, Mater. Sci. Eng. A. 820 (2021) 141512.

[28] S.B. Wang, D.L. Wu, H. She, M.X. Wu, D. Shu, A.P. Dong, H.C. Lai, B.D. Sun, Design of high-ductile medium entropy alloys for dental implants, Mater. Sci. Eng. C-Mater. Biol. Appl. 113 (2020) 10.

[29] T.D. Huang, S.Y. Wu, H. Jiang, Y.P. Lu, T.M. Wang, T.J. Li, Effect of Ti content on microstructure and properties of TixZrVNb refractory high-entropy alloys, Int. J. Miner. Metall. Mater. 27 (10) (2020) 1318–1325.

[30] Z.B. An, S.C. Mao, T. Yang, C.T. Liu, B. Zhang, E. Ma, H. Zhou, Z. Zhang, L.H. Wang, X.D. Han, Spinodal-modulated solid solution delivers a strong and ductile refractory high-entropy alloy, Mater. Horizons 8 (3) (2021) 948–955.

[31] S. Laube, A. Kauffmann, S. Schellert, S. Seils, A.S. Tirunilai, C. Greiner, Y.M. Eggeler, B. Gorr, H.-J. Christ, M. Heilmaier, Formation and thermal stability of two-phase microstructures in Al-containing refractory compositionally complex alloys, Sci. Technol. Adv. Mater. 23 (1) (2022) 692–706.

[32] S.Y. Wang, F.C. Lang, Y.M. Xing, Geometric phase analysis for characterization of 3D morphology of carbon fiber reinforced composites, Compos. Sci. Technol. 242 (2023) 110215.

[33] M.J. Hÿtch, E. Snoeck, R. Kilaas, Quantitative measurement of displacement and strain fields from HREM micrographs, Ultramicroscopy 74 (3) (1998) 131–146.

[34] F. Findik, Improvements in spinodal alloys from past to present, Mater. Des. 42 (2012) 131–146.

[35] B.L. Yin, F. Maresca, W.A. Curtin, Vanadium is an optimal element for strengthening in both fcc and bcc high-entropy alloys, Acta. Mater. 188 (2020) 486–491.

[36] M. Kato, Hardening by spinodally modulated structure in b.c.c. alloys, Acta. Metall. 29 (1) (1981) 79–87.

[37] T. Xin, Y. Zhao, R. Mahjoub, J. Jiang, A. Yadav, K. Nomoto, R. Niu, S. Tang, F. Ji, Z. Quadir, D. Miskovic, J. Daniels, W. Xu, X. Liao, L.-Q. Chen, K. Hagihara, X. Li, S. Ringer, M. Ferry, Ultrahigh specific strength in a magnesium alloy strengthened by spinodal decomposition, Sci. Adv. 7 (23) (2021) eabf3039.

[38] Y.Q. Bu, Y. Wu, Z.F. Lei, X.Y. Yuan, H.H. Wu, X.B. Feng, J.B. Liu, J. Ding, Y. Lu, H. T. Wang, Z.P. Lu, W. Yang, Local chemical fluctuation mediated ductility in body-centered-cubic high-entropy alloys, Mater. Today. 46 (2021) 28–34.

[39] Q. Wu, F. He, J. Li, H.S. Kim, Z. Wang, J. Wang, Phase-selective recrystallization makes eutectic high-entropy alloys ultra-ductile, Nat. Commun. 13 (1) (2022) 4697.

[40] H. Yang, K. Li, Y. Bu, J. Wu, Y. Fang, L. Meng, J. Liu, H. Wang, Nanoprecipitates induced dislocation pinning and multiplication strategy for designing high strength, plasticity and conductivity Cu alloys, Scr. Mater. 195 (2021) 113741.

[41] I.A. Su, K.K. Tseng, J.W. Yeh, B. El-Sayed, C.H. Liu, S.H. Wang, Strengthening mechanisms and microstructural evolution of ductile refractory medium-entropy alloy Hf20Nb10Ti35Zr35, Scr. Mater. 206 (2022) 6.

[42] Y. Lu, Y.H. Zhang, E. Ma, W.Z. Han, Relative mobility of screw versus edge dislocations controls the ductile-to-brittle transition in metals, Proc. Natl. Acad. Sci. U. S. A. 118 (37) (2021) 6.

[43] Q.Q. Ding, Y. Zhang, X. Chen, X.Q. Fu, D.K. Chen, S.J. Chen, L. Gu, F. Wei, H.B. Bei, Y.F. Gao, M.R. Wen, J.X. Li, Z. Zhang, T. Zhu, R.O. Ritchie, Q. Yu, Tuning element distribution, structure and properties by composition in high-entropy alloys, Nature 574 (7777) (2019) 223–227.

[44] S. Zhao, R. Zhang, Y. Chong, X. Li, A. Abu-Odeh, E. Rothchild, D.C. Chrzan, M. Asta, J.W. Morris, A.M. Minor, Defect reconfiguration in a Ti–Al alloy via electroplasticity, Nat. Mater. 20 (4) (2021) 468–472.

[45] T. Li, S. Wang, W. Fan, Y. Lu, T. Wang, T. Li, P.K. Liaw, CALPHAD-aided design for superior thermal stability and mechanical behavior in a TiZrHfNb refractory high-entropy alloy, Acta. Mater. 246 (2023) 118728.

[46] M. Stricker, D. Weygand, Dislocation multiplication mechanisms – Glissile junctions and their role on the plastic deformation at the microscale, Acta. Mater. 99 (2015) 130–139.

[47] F. He, S. Wei, J.L. Cann, Z. Wang, J. Wang, C.C. Tasan, Composition-dependent slip planarity in mechanically-stable face centered cubic complex concentrated alloys and its mechanical effects, Acta. Mater. 220 (2021) 117314.

[48] Z.F. Lei, X.J. Liu, Y. Wu, H. Wang, S.H. Jiang, S.D. Wang, X.D. Hui, Y.D. Wu, B. Gault, P. Kontis, D. Raabe, L. Gu, Q.H. Zhang, H.W. Chen, H.T. Wang, J.B. Liu, K. An, Q.S. Zeng, T.G. Nieh, Z.P. Lu, Enhanced strength and ductility in a high-entropy alloy via ordered oxygen complexes, Nature 563 (7732) (2018) 546–550.

[49] R. Wang, Y. Tang, Z. Lei, Y. Ai, Z. Tong, S. Li, Y. Ye, S. Bai, Achieving high strength and ductility in nitrogen-doped refractory high-entropy alloys, Mater. Des. 213 (2022) 110356.